Forcing Conditions of Cross-Shelf Plumes on a Wide Continental Shelf, Winyah Bay, South Atlantic Bight

Steven L. Dykstra[1,2*], Gabrielle Ricche[2,3], George Marmorino[4] and Alexander E. Yankovsky[2]

[1]College of Fisheries and Ocean Science, University of Alaska Fairbanks, Fairbanks, AK 99775.

[2]School of Earth, Ocean, and Environment, University of South Carolina, Columbia, SC 29208.

[3]Now at Rosenstiel School of Marine, Atmospheric & Earth Science, University of Miami, Miami, FL, 33149.

[4]Remote Sensing Division, U.S. Naval Research Laboratory, Washington, DC 20375.

Corresponding Author: Steven L. Dykstra (sdykstra@alaska.edu)

Highlights:

- Cross-shelf plumes are formed by light-to-moderate upwelling favorable winds
- Stronger winds shut down the estuarine outflow separation from the coastline
- High river discharge reduces the optimal wind stress range for cross-shelf plumes

Key Words: river plume, upwelling, South Carolina, Gulf Stream, wind stress, cross-shelf

Abstract

Buoyant cross-shelf river plumes can extend far offshore through the combined effect of buoyancy and wind forcing, creating a critical land-ocean link in global biogeochemical cycles. On the Carolinas continental shelf, cross-shelf plume structure has been analyzed using satellite imagery, with forcing conditions represented by an estuarine Richardson number, wind stress, and alongshore pressure gradient. Three distinct cross-shelf plume patterns emerged, each occurring under an upwelling-favorable wind: (1) The separated plume, when a single filament of buoyant water spreads offshore (a prototypical cross-shelf plume structure); (2) The upwind-curving plume, which turns against the wind at some offshore distance and is created by stronger buoyancy forcing; and (3) The multi-lobe plume, which is partially trapped by the coast with multiple streaks protruding offshore and is created by stronger wind forcing, and further aided by a coincident alongshore pressure gradient force. The latter two regimes represent a low-wind, high discharge limit and a strong-wind limit of cross-shelf plumes. High-resolution satellite

images reveal rich submesoscale variability associated with each plume type. Results suggest plume transport may extend farthest offshore in low-energy separated plumes through a balance of weak buoyancy and weak wind forcing.

1 Introduction

Globally, rivers represent a major pathway for the delivery of terrigenous material (both dissolved and suspended) into a coastal ocean. Most material fate is local to continental shelves, such as the 100-km wide South Atlantic Bight which separates local river mouths in the southeastern United Sates from the Gulf Stream (Bane et al., 1981). The partitioning of river-borne nutrients between coastal and open-ocean consumption by primary production is addressed in several recent studies (e.g., Sharples et al., 2017; Izett and Fennel, 2018a, b). In these papers, the authors link the offshore transport of nutrients to the dynamics of coastal plumes. How these nutrients extend across broad continental shelfs to global ocean currents is critical to our understanding of biogeochemical cycles (Bauer et al., 2013; Horner-Devine et al., 2015).

One pattern of the coastal plume formation particularly efficient for cross-shelf exchange was recently described by Yankovsky et al. (2022) and Yankovsky and Yankovsky (2024), where it is referred to as a cross-shelf plume. The cross-shelf plumes are characterized by an elongated, filament-like structure with length-to-width aspect ratio reaching $O(10)$. They are generated by light-to-moderate upwelling-favorable winds which transport buoyant water offshore without substantial entrainment of the ambient shelf water. However, formation of cross-shelf plumes is not just an externally-forced advective process, as those plumes exhibit intrinsic dynamics as well—which maintain their tight transverse dimension and arise from their supercritical regime (in terms of the internal Froude number) (Yankovsky and Yankovsky, 2024). The supercritical regime is sustained over long cross-shelf distances due to a superposition of the buoyancy-driven plume circulation and the wind-induced surface currents (Yankovsky et al., 2022). The advection of buoyancy-driven momentum by wind-induced currents prevents the geostrophic adjustment within the plume and leads to the continuous radiation of internal solitons from plume’s downwind edge into the plume, in the upwind direction (Yankovsky and Yankovsky, 2024). As a result of this internal wave radiation, the plume accumulates buoyant water on the upwind side and exhibits minimal downwind diffusion.

In this work we analyze satellite images of cross-shelf plumes off Winyah Bay in several frequency bands representing various seawater properties over time span from 2017 through early 2020. We then assess forcing conditions preceding the observed events. The forcing comprises the freshwater discharge, its tidal mixing in the estuary and the wind stress operating on the continental shelf. The combination of freshwater discharge and tides defines properties of the buoyant outflow and can be represented by the estuarine Richardson number (Ri_E) following Nash et al. (2009). The role of wind stress is twofold: (i) vertical mixing determined by the wind stress magnitude, and (ii) advection of buoyant water by offshore Ekman transport and alongshore geostrophic circulation, both controlled by the alongshore wind stress component. The rest of the paper is organized as follows. Section 2 describes the data and their processing, as well as physical hypotheses governing the analysis. Sections 3 presents, interprets and discusses the results, while section 4 concludes the paper.

2 Data and Methods

2.1 Study Site and Data Sources

The South Atlantic Bight is a broad (~100 km) shelf with a gentle (~$5x10^{-4}$) slope along the southeastern United States (Figure 1). At the shelf break, the Gulf Stream flows northward (Bane et al., 1981). Terrestrial waters and nutrients enter through numerous rivers, making the shelf a relatively diffuse region of freshwater influence—governed by buoyancy, Coriolis, wind stress, and bed friction—and is noted for being sediment deprived (McCarney-Castle et al., 2010; Patchineelam et al. 1999). The largest freshwater source is Winyah Bay, which commonly ranges 100-1,400 m^3s^{-1} (5^{th}-95^{th} percentile) and has a mean river discharge $\overline{Q_r}$ of 510 m^3s^{-1} (2007-2021). The watershed area A_w is 47,060 km^2 and includes the Pee Dee River ($\overline{Q_r}$: 390 m^3s^{-1}, A_w: 36,520 km^2), the Waccamaw River ($\overline{Q_r}$: 50 m^3s^{-1}, A_w: 3,730 km^2), and the Black River ($\overline{Q_r}$: ~50 m^3s^{-1}, A_w: 4,040 km^2) (Figure 2a). Winyah Bay is a partially mixed estuary (Kim & Voulgaris, 2005) with semidiurnal tides that range 0.94-1.54m. At subtidal frequencies, salinity is strongly influenced by river discharge (Figure 2b). Exiting Winyah Bay through a narrow navigational channel flanked by jetties, the plume is commonly supercritical, based on the internal Froude number, and surface trapped (e.g., Yankovsky & Voulgaris, 2019; Yankovsky et al., 2022).

Satellite images of the Winyah Bay plume were collected from the NOAA CoastWatch East Coast Node website (https://coastwatch.chesapeakebay.noaa.gov/region_cl.php) to inform a planned field campaign in March 2020 (Yankovsky et al., 2022) focused on the offshore transport of the Winyah Bay plume water. A set of 40 events spanning time interval from January 2017 through January 2020 was initially selected using the following criteria: visible detachment from the coast and offshore spreading of the plume seen in multiple frequency bands (e.g., sediment index, chlorophyll, turbidity, true color, etc.). Some events included imagery for several consecutive days. At the time of image selection, no assumptions were made regarding the dynamics or forcing conditions. Many image products revealed elongated, filament-like structures separating from the coast and crossing the shelf at various angles, from gently oblique to near normal. A subset of 15 events was then selected that illustrated the variety of forms this cross-shelf plume structure could take.

These 15 events are the basis for this study. Each event is referred to by the single, most representative day if multiple day imagery is available. For instance, temporal evolution of the event on January 31, 2017 is discussed by Yankovsky and Yankovsky (2024), their Figure 17. For this study, the images are level 2 products of remote sensing reflectance (Rrs) at 667 and 671 nm from MODIS Aqua L2 and VIIRS SNPP L2, respectively—proxies for suspend sediment—and the associated chlorophyll-a products—proxies for biological productivity (https://oceancolor.gsfc.nasa.gov/cgi/browse.pl?sen=amod). Both are commonly used to capture plume structure (e.g., Barnes et al., 2015; Dzwonkowski et al., 2015; Stumpf and Pennock, 1989). For categorizing various structures of cross-shelf plumes (section 3.1), additional frequency bands were utilized as proxies for turbidity and particulate organic carbon (see Supporting Information). Fine details of the plume structure were characterized on select days using satellite data collected by the Sentinel-2 MultiSpectral Instrument (https://scihub.copernicus.eu) and the Landsat 8 Operational Land Imager (https://earthexplorer.usgs.gov).

Timeseries observations were accessed from the United States Geological Survey (USGS) for river discharge data (stations: 02135200, 02110704, 02136030), the National Oceanic and Atmospheric Administration (NOAA) National Data Buoy Center (NDBC) for wind (station: 41013) and water level data (stations: 8661070, 8658163), and the National Estuary Research Reserve (NERR) for estuary data (station: NIWWSWQ; Table 1). The estuary water level and surface salinity data are collected 113 km downstream of the Pee Dee River station (02135200) where the estuary channel width is 1.2 km, similar to the estuary mouth (1.4 km) 17 km further downstream. Spatial data for ground elevation came from the shuttle radar topography mission (SRTM+, Farr et al., 2007).

2.2 Assumptions on the governing dynamics

Our analysis is based on several assumptions about the leading-order dynamics which result in the formation of cross-shelf plumes. The buoyant outflow from Winyah Bay is determined by the freshwater discharge and the estuarine tidal mixing, which jointly control the volumetric transport, salinity anomaly, and velocity of buoyant outflow through the mouth. This buoyancy forcing can be represented as the estuarine Richardson number (Fischer 1972, Nash et al. 2009):

$$Ri_E = g' \frac{Q_r}{W U_t^3} \quad (1),$$

where g' is the reduced gravitational acceleration associated with the freshwater density ρ anomaly relative to the ambient seawater on the shelf ρ_0 with salinity of 34 ($g' = g(\rho - \rho_0)\rho_0^{-1}$, g is gravity), assumed to have a constant value of 0.25 m s^{-2}; Q_r is the river discharge; W is the estuary width (1.2 km); and U_t is the peak tidal velocity. Because direct velocity measurements are not available, U_t is inferred from tidal gauge data assuming that semi-diurnal tidal species propagate in the form of long gravity waves:

$$U_t \approx \eta_t \sqrt{\frac{g}{h}} \quad (2),$$

where η_t is the free surface tidal amplitude and h is the water depth (e.g., MacCready, 1999).

Next, we assume that the cross-shelf plume regime can be established under favorable wind forcing conditions when buoyant water is transported offshore beyond natural limits of the unforced plume. The primary mechanism is the Ekman transport associated with the alongshore wind stress component (e.g., Fong & Geyer, 2001; Lentz, 2004), which can only be established when the Ekman layer is shallower than the local water depth. This implies that surface and bottom boundary layers should remain separated in the vertical, and the wind-induced turbulence cannot overcome stratification of the buoyant layer. In this regard, two elements of the wind forcing will be analyzed: the alongshore wind stress responsible for the Ekman transport, and the magnitude of the wind stress responsible for the vertical mixing.

Lastly, wind-induced advection of the buoyant layer is more complex than the offshore Ekman transport alone, and includes the alongshore wind-driven current (e.g., Yankovsky & Yankovsky, 2024). Under simplifying assumptions of the uniform alongshore topography and steady-state wind, the alongshore current is driven by the cross-shore pressure gradient through the geostrophic balance. The cross-shore pressure gradient arises from the Ekman transport divergence nearshore and is proportional to the alongshore wind stress. However, under more realistic conditions of 2-dimensional topography and/or non-uniform wind forcing, alongshore current can also be affected by the alongshore pressure gradient (APG) (e.g., Carton, 1984). APG is established after the passage of continental shelf waves propagating in the direction of the Kelvin wave phase (hereinafter, referred to as downstream), originating at the upstream edge of the forcing area. In this regard, the change in coastline orientation is similar to the change of the alongshore wind stress (e.g., Crépon et al., 1984). The APG force typically (but not always) opposes the alongshore wind stress component, and can substantially reduce (or even reverse) the alongshore current. Hence, the APG will also be analyzed as a possible contributor to the alongshore advection of the buoyant water.

2.3 Data analysis

Timeseries data were analyzed for wind stress, APG and Ri_E. For wind stress, the drag coefficient C_d is nonlinear following Trenberth et al. (1990). The along-shore and cross-shore wind stresses are defined at 40º and 130º from north, respectively. APG is approximated using the water level difference between Myrtle Beach and Wilmington (~140 km, Figure 1) such that its positive value corresponds to the APG force pointing upstream. All time series are low-pass filtered with a 40-hour Lanczos filter (e.g., Dzwonkowski et al., 2015) to represent subinertial dynamics.

Discharge from inland observations—where rivers are accurately measured—need corrections to represent the magnitude and timing of river effects near the coast (Dykstra & Dzwonkowski, 2020). Corrections for river discharge magnitude were made by low-pass filtering the tidal variability of each record and summing the most complete records (Pee Dee River and Waccamaw River). To approximate downstream sources and unaccounted tributaries, the magnitude was multiplied by the ratio of total watershed area to monitored watershed area (e.g., Dykstra & Dzwonkowski, 2021). To approximate river discharge timing near the estuary mouth, ln(Q_r) and salinity were cross-correlated with temporal offsets at 1 hour intervals. The best relationship was with Q_r lagged 22 hours (R^2=0.86; Figure 3), and even though R^2 was the same value to 60 hours, the cross-covariance grew weaker with time. For discharge magnitude effects on the temporal offset, a sensitivity test of binning events by size showed little change for all but extreme events. The 22-hour lag time suggests a river wave celerity of ~1.5 m s^{-1}, an expected value for a river-marine transition under non-flooding conditions (Dykstra & Dzwonkowski, 2020). Because flooding can delay and attenuate river events, subsequently affecting river plume dynamics (Dykstra & Dzwonkowski, 2020), we limit our analysis to discharges with in-channel flow. The peak tidal velocity in (1) is calculated from a timeseries of the Greater Diurnal Tidal Range (i.e., $2\eta_t$) which is determined by finding the daily high tide and daily low tide, spline fitting each, and finding the difference.

3 Results and Discussion

3.1 Observations of Plume Structure

Remote sensing reflectance and satellite derived chlorophyll-a observations of the Winyah Bay plume were sorted and compared to forcing conditions. Sorting the records for visible cross-shelf plumes, i.e., cloudless and distinct from background ambient shelf conditions, yielded fifteen representative examples (Figures 4, 5). The events cover all four seasons and have consistent structures in the satellite imagery of many bands (see also Kd490 and POC in the Supporting Information Figures S1, S2).

All cases correspond to the upwelling favorable wind stress at and prior to observations (vectors, Figures 4, 5). All images exhibit elongated filaments extending offshore from the coast, but their size, orientation, and number varies widely between the cases, as described in section 2.1. To facilitate discussion of forcing conditions, we distinguish three specific patterns of cross-shelf plumes. A prototypical cross-shelf plume comprises a series of tidal sub-plumes aligned as a single streak of buoyant water which detaches from the coast at the mouth. It extends upstream (e.g., northward) and offshore, and is referred to as a separated plume (Figures 4g-l, 5g-l).

In some cases, there are more than one streak of buoyant water protruding offshore and originating not only from the mouth, but also from coastline farther upstream. This happens when the plume is partially trapped by the coast, such that more than one tidal pulse maintain contact with the coastline. This structure is referred to as multi-lobe plumes (Figures 4a-f, 5a-f).

For instance, cases "b" and "i" look somewhat similar, but the former remains attached to the coast upstream from the mouth, while the latter is detached, so they are categorized as multilobe and separated, respectively.

Finally, upwind-curving plumes (Figures 4m-o, 5m-o) turn anticyclonically and spread against the wind, so that the plume at its maximum offshore extension still resides at the alongshore coordinate of the mouth. Recalling that the alongshore coordinate is defined as 40 deg from true north, this implies that the offshore tip of the plume crosses the line running from the mouth at 130 deg from true north.

3.2 Plume Forcing Conditions

The unique plume forcing conditions are further examined to describe plume structure based on external parameters. We explain the logic of our analysis by first focusing on the conditions preceding one example: a characteristic separated plume observed July 8, 2017 at 19:00 (Figures 4h, 5h). The instantaneous wind stress magnitude was variable and doubled 2-3 days before the satellite observation (thin lines, Figure 6a). Nearly all the wind stress was accounted for in the along-shelf component. The low-passed along-shelf wind stress, known to control Ekman transport and cross-shore circulation (Gill, 1982), was consistently positive, indicating stable upwelling conditions and offshore surface transport. The wind stress was counteracted by the alongshore pressure gradient (APG), shown here using a water level difference (Figure 6a). Similar consistency was observed in the Estuary Richardson number due to relatively steady river discharge and maximum tidal velocity conditions (Figure 6b). The relatively low river discharge to tidal velocity ratio (Ri_E~0.07) indicates weak estuary stratification. The external forcing conditions of each plume were summarized using the 3-day averages of wind stress, Ri_E, and the water level difference preceding satellite observations. Because the image acquisition times varied over a two-hour period (17:24-19:18 UTC) and plume responses to wind action having a several-hour time lag (Qu & Hetland, 2019), for simplicity, means were taken from 12:00 3 days before observation day to 12:00 of observation day (e.g., gray area, Figure 6a, b).

Forcing conditions are summarized for the 15 cases in Figure 7 and Table S1. The most important agents—the buoyant outflow and the upwelling-favorable wind stress component (Fig. 7a)—reveal that cross-shelf plumes are formed under light-to moderate wind stress: the average value of its alongshore component is less than 0.1 Pa. The upwind curving plumes tend to form, when the buoyancy forcing is large (higher values of Ri_E), while the upwelling favorable wind is relatively weaker. For weak winds, high Ri_E delineates most upwind curving plumes from low Ri_E separated plumes. The strongest alongshore winds produce multi-lobe plumes, although there is no clear separation between multi-lobe and other types in Figure 7a.

This pattern can be explained by the partial trapping of multi-lobe plumes nearshore, through the inner-shelf regime. This regime requires stronger vertical mixing, which is proportional to the total wind stress magnitude, not just its alongshore component: Figure 7b shows a better separation between multi-lobe and other types of cross-shelf plumes, especially when both the mean and standard deviation are considered (i.e., right extent of bars). However, even in this diagram there is some ambiguity represented by cases d, e (both are multi-lobe) and n (upwind-curving), the latter corresponding to a stronger averaged wind stress, although all three have comparable wind stress variations over a three-day period. This feature can be reconciled, when the third forcing factor is taken into account, the APG force (Fig. 7c). As expected, in the majority of cases the APG force points downstream, against the alongshore wind stress. One of the strongest APG is seen in case n, thus preventing the upstream advection along the coast, and the formation of the multi-lobe plume. On the other hand, cases d and e are characterized by a less common situation, when the APG force coincides with the alongshore wind stress orientation, which promotes advection of the buoyant water upstream along the coast.

3.3 High-resolution Images

We conclude the analysis of satellite imagery with high-resolution images of cross-shelf plumes; one of each plume type and one in the early stages of cross-shelf plume formation. The separated and upwind curving plume images (Fig. 8a and b, respectively) correspond precisely to the events presented in Figure 4 (cases n and j, respectively) and the multi-lobe plume image is obtained two days earlier than case b, on February 11, 2017 (Fig. 8c). The last image corresponds to the shipboard measurements collected on March 11, 2020, reported by Yankovsky et al. (2022; Fig. 9).

In a highly simplified interpretation, the cross-shelf plume can be considered as a train of tidal pulses (or sub-plumes) aligned along the direction of the wind-induced drift and kept together by mixing processes occurring at interior fronts separating sub-plumes (Yankovsky &

Voulgaris, 2019; Yankovsky et al., 2022). Similar structure is seen in Figure 8a, where three distinctive sub-plumes can be recognized (marked with numbers 1-3). The first, nearest to the mouth, is the newly discharged tidal plume, with concentric rings. While the exact nature of these rings cannot be established due to a lack of simultaneous in situ measurements, the modeling of Marmorino and Evans (2021) suggests these frequently seen features are generated by shear instabilities. Separation of the plume from the coast is also clearly seen in this image. Figure 8b corroborates the curving-back plume structure of case n as the two images look nearly identical (Figures 8b, 4n). While the plume's upstream (downwind) edge in Fig. 4 appears diffuse, the high-resolution image reveals a sharp front around most of the plume circumference, except for its nearshore part, consistent with recent modeling study (Yankovsky & Yankovsky, 2024). Case b on February 13, 2017 represents the multi-lobe structure, when the plume is partially trapped at the coastline upstream from the mouth. At the time of the high-resolution image on February 11, the upwelling-favorable wind has already been operating (Fig. 8c). The plume spreads along the coast over some distance upstream (northward), then sharply turns offshore retaining its distinct elongated shape. All three high resolution examples (Fig. 8a-c) reveal rich submesoscale variability associated with cross-shelf plumes, as was also found in the high-resolution model runs of Yankovsky and Yankovsky (2024).

Finally, we revisit the event on March 11, 2020, which is not included in the 15 cases discussed here. According to Yankovsky et al., 2022, the observed plume represented an early stage of the cross-shelf plume formation: it had all the requisites of such a plume, but lacked an elongated shape, because the upwelling favorable wind operated for less than two days by the end of the survey. Nevertheless, the plume extended offshore for more than 30 km as inferred from the shipboard data and even farther, according to a satellite image (Fig. 2 in Yankovsky et al., 2022). As mentioned in the introduction, the maintenance of the cross-shelf plume regime occurs (at least in part) through the upwind (in this case, southward) radiation of internal waves; reducing the downwind diffusion of buoyant water. The evidence for such waves is presented in Figure 9 (arrows). Unlike the modeling results by Yankovsky and Yankovsky (2024) where internal waves remain trapped within the plume due to unstratified ambient shelf flow, here the shelf water has some ambient stratification, so that internal waves leak outside of the plume. It should be emphasized, that these internal waves originate neither at the mouth nor at the shelfbreak, two principal sources of internal wave energy previously reported in numerous publications (e.g., Jackson, 2004; Nash & Moum, 2005; Wright & Coleman, 1971). While Yankovsky et al. (2022) deduced the presence of internal waves from elevated values of TKE dissipation below the plume and away from the mouth, as well as from the vertical phase propagation in band-passed current measurements, Figure 9 provides direct observational evidence for internal wave radiation during this event occurring in the upwind (southward) direction—providing maintenance of the cross-shelf plume regime.

3.4 Discussion

Our analysis reveals that the formation of cross-shelf plumes is based on a delicate balance between buoyancy forcing of the estuarine outflow, nearshore mixing producing the inner-shelf regime (e.g., Lentz, 1995), and wind-induced transport—both offshore and along-shore. The inner-shelf dynamics are characterized by a merging of surface and bottom boundary layers, the former being primarily wind driven, and the latter resulting from the combined action of tides, waves, and low-frequency currents (e.g., Lentz & Fewings, 2012). Increasing wind stress expands the inner-self regime offshore, such that the discharged buoyant water remains within the inner-shelf and cannot be advected offshore by means of the Ekman transport (see annotated diagram of Figure 4a-f in Figure 10a). Because the estuarine discharge is time dependent (modulated by tides), the most energetic part of the ebbing outflow can episodically escape the inner-shelf area, thus forming multiple filaments of buoyant water (Yankovsky & Yankovsky, 2024). Similar episodic pulsing detachments can be formed by fluctuations in wind forcing. Overall, we conclude that strong wind stress shuts down the cross-shelf plume regime. It should also be noted that in many areas of the world ocean tides are the primary driver of the bottom boundary layer, and the bottom-induced turbulence can significantly affect the plume even without the wind forcing (Spicer et al., 2021). Hence, even moderate winds can trap an estuarine outflow in the inner-shelf regime in the presence of tidal mixing.

Both separated (cases g, i, j, l) and upwind-curving plumes exhibit anticyclonic turning of the buoyancy-driven jet as it crosses the shelf (Figures 4, 10b, c). This can be associated with the lateral shear of the wind-driven alongshore current which tends to decay offshore (e.g., Brink, 1991), but can also be due to the Coriolis effect on a free jet (e.g., Avicola & Huq, 2003). In general, the anticyclonic turning makes the shelf crossing more efficient, when the plume approaches a normal angle with the shelf orientation (as in cases j, m, and n). However, as the balance between the wind-induced advection and the buoyancy forcing shifts towards buoyancy, a free jet can curve back toward the coast (which appears to happen in case o). For this reason, upwind-curving plumes represent a limiting case of the cross-shelf plume regime, when the buoyancy dominates and the plume can potentially evolve into a conventional anticyclonic bulge (e.g., Avicola & Huq 2003; Dzwonkowski et al., 2015).

Due to their elongated shape, cross-shelf plumes can develop quickly and reach the outer shelf (or even the shelf break) in a matter of several days. In 6 cases, the upwelling favorable wind started after the beginning of the nominal 3-day averaging period (that is, lasted less than 3 days). These events are b, d, e (multi-lobe plumes) and m, n, o (all upwind-curving plumes). In the perhaps most dramatic case, case j, the upwelling-favorable wind was insignificant (~0.02 Pa) prior to the 3-day averaging interval. The other separated plumes, with their low energy forcing conditions, demonstrate that—by constraining the plume volume in a long filament—low river discharge and weak upwelling winds can efficiently transport terrestrial nutrients to the shelf break.

The cross-shelf transport limits of wind stress and buoyancy forcing—observed in the multi-lobe and upwind-curving plumes (Figure 4)—may constrain the fate of terrigenous materials near the coast. The associated high river discharges and winds reduce estuary residence times and resuspend bed materials, making plume nutrients relatively more bioavailable and/or abundant (Bauer et al. 2013; Hopkinson & Vallino, 1995). While the high energy conditions may enhance river-ocean links and biogeochemical cycling (e.g., Sharples et al., 2017; Izett and Fennel, 2018a, b), the high energy transport limits may constrain rapid cycling near the coast. Instead, lower energy separated plumes consistently transport lower bioavailable nutrients to the shelf break and Gulf Stream. Overall, the more critical forcing conditions for cross-shelf exchange were light to medium winds. This may partially explain how the predominantly downwelling Gulf of Alaska transforms into one of the most productive regions of the world as a nutrient rich region of freshwater influence is spread offshore by seasonal upwelling favorable winds that are surprisingly light (Rogers-Cotrone et al., 2008; Weingartner et al., 2005).

4 Conclusion

Cross-shelf plume structures off Winyah Bay are repeatedly seen in various satellite products suggesting their forcing conditions are ubiquitous. Using several years of satellite observations, we found that all cross-shelf plumes were surprisingly forced by upwelling favorable winds. Light to moderate winds are the most effective cross-shelf plume forcing conditions, creating separated plumes, detached from the coast. Excessive wind stress shut down the coastal detachment of the buoyant layer from the coast, advecting multi-lobe plumes alongshore. The multi-lobe plume represents a strong-wind limit of the cross-shelf plume. A large river discharge, weaker wind or shorter wind duration shift a competition between wind and buoyancy forcing towards buoyancy dominance, and the upwind-curving plume pattern emerges. The upwind-curving plume represents a low-wind limit of the cross-shelf plume. The separated plumes represent archetypical cross-shelf plumes while cross-shelf advection in the multi-lobe and upwind curing plumes are limited by partial trapping and curving back toward shore, respectively. Overall, cross-shelf plumes develop fast, over a period of several days (2.5-4). Lastly, the identification of a new class of cross-shelf plume structure and methods using satellite images and easily calculated forcing conditions make this study novel.

Acknowledgments

This research was funded through the University of South Carolina Advanced Support Program for Innovative Research Excellence-II. AY was supported by the US National Science Foundation award OCE-2148480. G. Marmorino was funded by the Office of Naval Research. We are unaware of any perceived financial conflicts of interests or affiliations.

References

Avicola, G., and P. Huq (2003). The characteristics of the recirculating bulge region in coastal buoyant outflows. *J. Marine Res*., **61**, 435-463.

Bane, J. M., Brooks, D. A., & Lorenson, K. R. (1981). Synoptic observations of the three-dimensional structure and propagation of Gulf Stream meanders along the Carolina continental margin. *Journal of Geophysical Research*, *86*(C7), 6411–6425. https://doi.org/10.1029/jc086ic07p06411

Barnes, B. B., Hu, C., Kovach, C., & Silverstein, R. N. (2015). Sediment plumes induced by the Port of Miami dredging: Analysis and interpretation using Landsat and MODIS data. *Remote Sensing of Environment*, *170*, 328–339. https://doi.org/10.1016/j.rse.2015.09.023

Bauer, J. E., Cai, W.-J., Raymond, P. A., Bianchi, T. S., Hopkinson, C. S., & Regnier, P. A. G. (2013). The changing carbon cycle of the coastal ocean. *Nature*, *504*(7), 61–70. https://doi.org/10.1038/nature12857

Brink, K.H. (1991). Coastal-Trapped Waves and Wind-Driven Currents Over the Continental Shelf. *Annu. Rev. Fluid Mech*, **23**, 389-412. https://doi.org/10.1146/annurev.fl.23.010191.002133

Carton, J. A. (1984). Coastal circulation caused by an isolated storm. *J. Phys. Oceanogr.*, **14**, 114-124.

Crépon, M., C. Richez, and M. Chartier, 1984: Effects of coastline geometry on upwellings. *J. Phys. Oceanogr*., **14**, 1365-1382.

Dykstra, S. L., & Dzwonkowski, B. (2021). The Role of Intensifying Precipitation on Coastal River Flooding and Compound River-Storm Surge Events, Northeast Gulf of Mexico. *Water Resources Research*, *57*(11). https://doi.org/10.1029/2020wr029363

Dykstra, S. L., & Dzwonkowski, B. (2020). The propagation of fluvial flood waves through a backwater-estuarine environment. *Water Resources Research*, *56*(2), e25743. https://doi.org/10.1029/2019wr025743

Dzwonkowski, B., Park, K., & Collini, R. (2015). The coupled estuarine-shelf response of a river-dominated system during the transition from low to high discharge. *Journal of Geophysical Research: Oceans*, *120*(9), 6145–6163. https://doi.org/10.1002/2015jc010714

Farr, T. G., Rosen, P. A., Caro, E., Crippen, R., Duren, R., Hensley, S., et al. (2007). The shuttle radar topography mission. *Reviews on Geophysics*, 45, RG2004. https://doi.org/10.1029/2005RG000183

Fong, D. A., & Geyer, W. R. (2001). Response of a river plume during an upwelling favorable wind event. *Journal of Geophysical Research: Oceans*, *106*(C), 1067–1084. https://doi.org/10.1029/2000jc900134

Gill, A. E., 1982. Atmosphere–Ocean Dynamics. Academic Press, 662 pp.

Horner-Devine, A. R., Hetland, R. D., & MacDonald, D. G. (2015). Mixing and Transport in Coastal River Plumes. *Annual Review of Fluid Mechanics*, *47*(1), 569–594. https://doi.org/10.1146/annurev-fluid-010313-141408

Hopkinson, C. S., & Vallino, J. J. (1995). The relationships among man's activities in watersheds and estuaries: a model of runoff effects on patterns of estuarine community metabolism. *Estuaries*, *18*(4), 598–621. https://doi.org/10.2307/1352380

Izett, J. G., & Fennel, K. (2018a). Estimating the Cross-Shelf Export of Riverine Materials: Part 1. General Relationships From an Idealized Numerical Model. *Global Biogeochemical Cycles*, *32*(2), 160–175. https://doi.org/10.1002/2017gb005667

Izett, J. G., & Fennel, K. (2018b). Estimating the Cross-Shelf Export of Riverine Materials: Part 2. Estimates of Global Freshwater and Nutrient Export. *Global Biogeochemical Cycles*, *32*(2), 176–186. https://doi.org/10.1002/2017gb005668

Jackson, C.R., 2004. An Atlas of Internal Solitary-like Waves and Their Properties. 2nd Ed. Global Ocean Associates, Alexandria, Virginia, 560pp. http://www.internalwaveatlas. com/Atlas2_index.html.

Lentz, S. (2004). The Response of Buoyant Coastal Plumes to Upwelling-Favorable Winds*. *Journal of Physical Oceanography*, *34*(11), 2458–2469. https://doi.org/10.1175/jpo2647.1

Lentz, S. J. (1995). Sensitivity of the Inner-Shelf Circulation to the Form of the Eddy Viscosity Profile. *Journal of Physical Oceanography*, *25*(1), 19–28. https://doi.org/10.1175/1520-0485(1995)025<0019:sotisc>2.0.co;2

Lentz, S. J., & Fewings, M. R. (2012). The Wind- and Wave-Driven Inner-Shelf Circulation. *Annual Review of Marine Science*, *4*(1), 317–343. https://doi.org/10.1146/annurev-marine-120709-142745

McCarney-Castle, K., Voulgaris, G., & Kettner, A. J. (2010). Analysis of Fluvial Suspended Sediment Load Contribution through Anthropocene History to the South Atlantic Bight Coastal Zone, U.S.A. *The Journal of Geology*, *118*(4), 399–416. https://doi.org/10.1086/652658

Nash, J. D., Kilcher, L. F., & Moum, J. N. (2009). Structure and composition of a strongly stratified, tidally pulsed river plume. *Journal of Geophysical Research: Oceans (1978–2012)*, *114*(C2). https://doi.org/10.1029/2008jc005036

Nash, J. D., and Moum, J. N. (2005). River plumes as a source of large amplitude internal waves in the coastal ocean. Nature 437, 400–403. doi: 10.1038/nature03936

Patchineelam, S. M., Kjerfve, B., & Gardner, L. R. (1999). A preliminary sediment budget for the Winyah Bay estuary, South Carolina, USA. *Marine Geology*, *162*(1), 133–144. https://doi.org/10.1016/s0025-3227(99)00059-6

Rogers-Cotrone, J., Yankovsky, A. E., & Weingartner, T. J. (2008). The impact of spatial wind variations on freshwater transport by the Alaska Coastal Current. *Journal of Marine Research*, *66*(6), 899–925. https://doi.org/10.1357/002224008788064603

Sharples, J., Middelburg, J. J., Fennel, K., & Jickells, T. D. (2017). What proportion of riverine nutrients reaches the open ocean? *Global Biogeochemical Cycles*, *31*(1), 39–58. https://doi.org/10.1002/2016gb005483

Spicer, P., Cole, K. L., Huguenard, K., MacDonald, D. G., & Whitney, M. M. (2021). The Effect of Bottom – Generated Tidal Mixing on Tidally Pulsed River Plumes. *Journal of Physical Oceanography*. https://doi.org/10.1175/jpo-d-20-0228.1

Stumpf, R. P., & Pennock, J. R. (1989). Calibration of a general optical equation for remote sensing of suspended sediments in a moderately turbid estuary. *Journal of Geophysical Research: Oceans*, *94*(C10), 14363–14371. https://doi.org/10.1029/jc094ic10p14363

Trenberth, K. E., Large, W. G., & Olson, J. G. (1990). The Mean Annual Cycle in Global Ocean Wind Stress. *Journal of Physical Oceanography*, *20*(11), 1742–1760. https://doi.org/10.1175/1520-0485(1990)020<1742:tmacig>2.0.co;2

Weingartner, T. J., Danielson, S. L., & Royer, T. C. (2005). Freshwater variability and predictability in the Alaska Coastal Current. *Deep Sea Research Part II: Topical Studies in Oceanography*, *52*(1–2), 169–191. https://doi.org/10.1016/j.dsr2.2004.09.030

Wright, L. D., & Coleman, J. M. (1971). Effluent expansion and interfacial mixing in the presence of a Salt Wedge, Mississippi River Delta. *Journal of Geophysical Research*, *76*(36), 8649–8661. https://doi.org/10.1029/jc076i036p08649

Yankovsky, A. E., & Voulgaris, G. (2019). Response of a coastal plume formed by tidally-modulated estuarine outflow to light upwelling-favorable wind Response of a coastal plume formed by tidally-modulated estuarine outflow to light upwelling-favorable wind. *Journal of Physical Oceanography*, *49*(3), 691–703. https://doi.org/10.1175/jpo-d-18-0126.1

Yankovsky, A. E., Fribance, D. B., Cahl, D., & Voulgaris, G. (2022). Offshore Spreading of a Supercritical Plume Under Upwelling Wind Forcing: A Case Study of the Winyah Bay Outflow. *Frontiers in Marine Science*, *8*. https://doi.org/10.3389/fmars.2021.785967

Yankovsky, E, and A. E. Yankovsky (2023). The cross-shelf regime of a wind-driven supercritical river plume. *Submitted to J. Phys. Oceanogr*.

Tables

Table 1. Data station locations, length of records and source agency.

Paramiter	Station Name	Station Number	Agency	Latitude	Longitude	Record
River Discharge	Pee Dee River at Bucksport	02135200	USGS	33.6608	-79.1547	2007-2022
	Waccamaw River at Conway	02110704	USGS	33.8328	-79.0439	2007-2022
	Black River near Andrews	02136030	USGS	33.4903	-79.5458	2017-2022
Wind	Frying Pan Shoals, NC	41013	NOAA NDBC	33.4410	-77.7640	2003-2022
Water Level / Salinity	Winyah Bay Surface	NIWWSWQ	NERRS	33.3094	-79.2888	2016-2022
Water Level	Springmaid Pier, SC	8661070	NOAA	33.6550	-78.9167	2016-2022
	Wrightsville Beach, NC	8658163	NOAA	34.2133	-77.7867	2016-2022

Figures

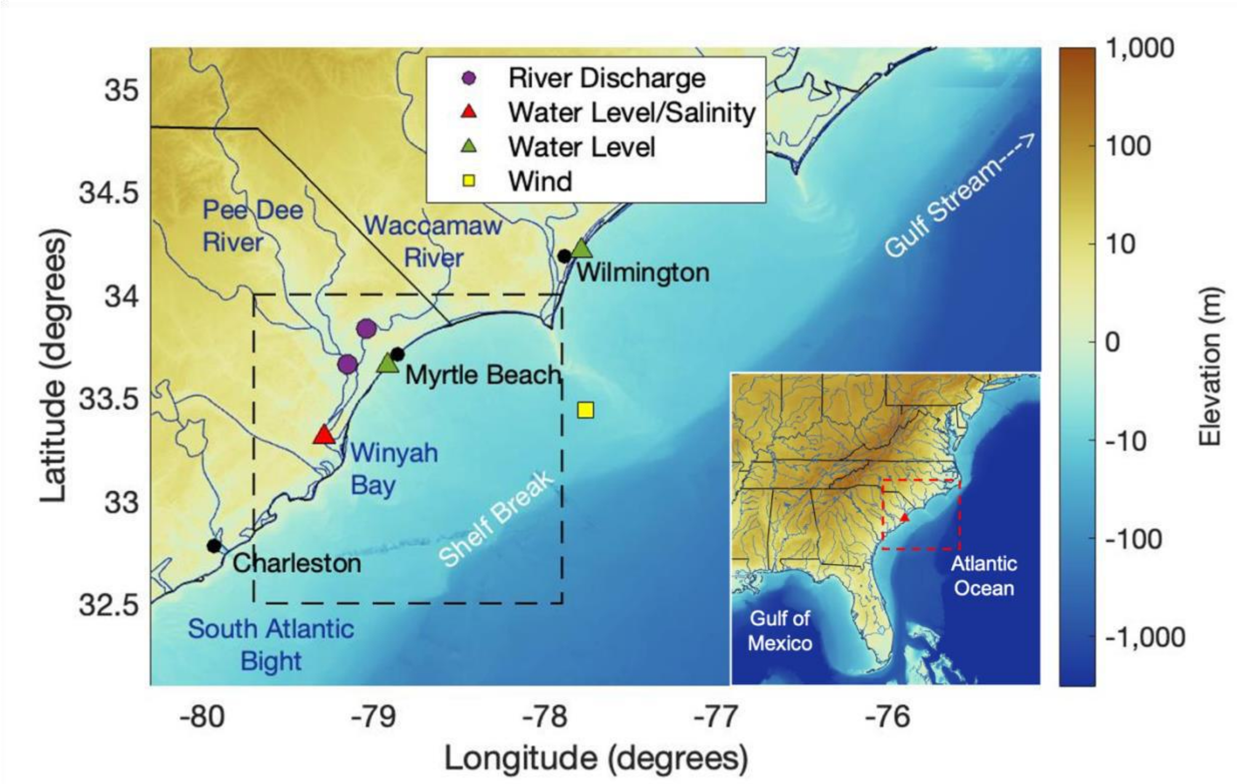

Figure 1. A map of the South Atlantic Bight in the Atlantic Ocean, showing the region along North and South Carolina. The red dashed line outlines Figure 1 and the black dashed line outlines Figure 4 and 5.

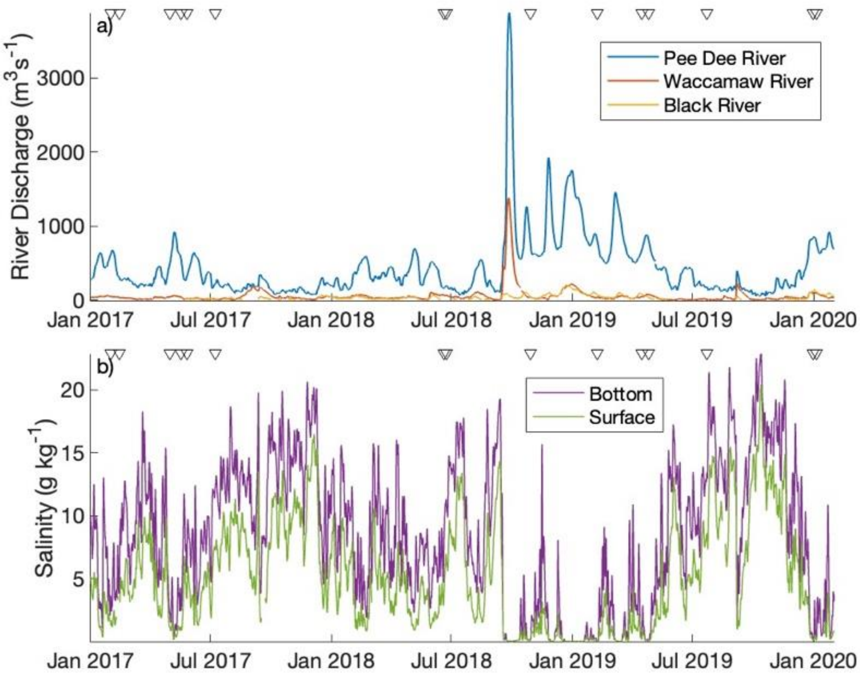

Figure 2. Timeseries of (a) the subtidal river discharge and (b) the salinity in Winyah Bay for the entire study period. Black triangles show the time of plume observations in Figures 4 and 5.

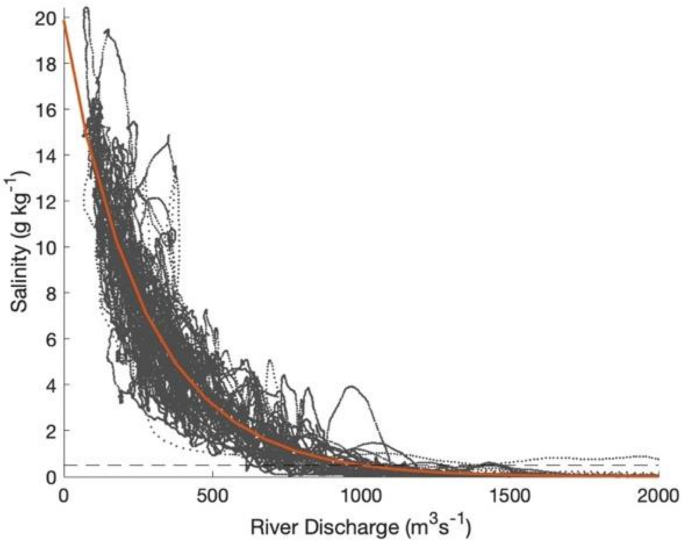

Figure 3. River discharge-salinity relationship for Winyah Bay using a 22-hour lagged river discharge and subtidal surface salinity. The fit (red line; $Salinity = 19.7e^{-Q_r/270}$) uses a minimum threshold of 0.5 g kg^{-1} (dotted line).

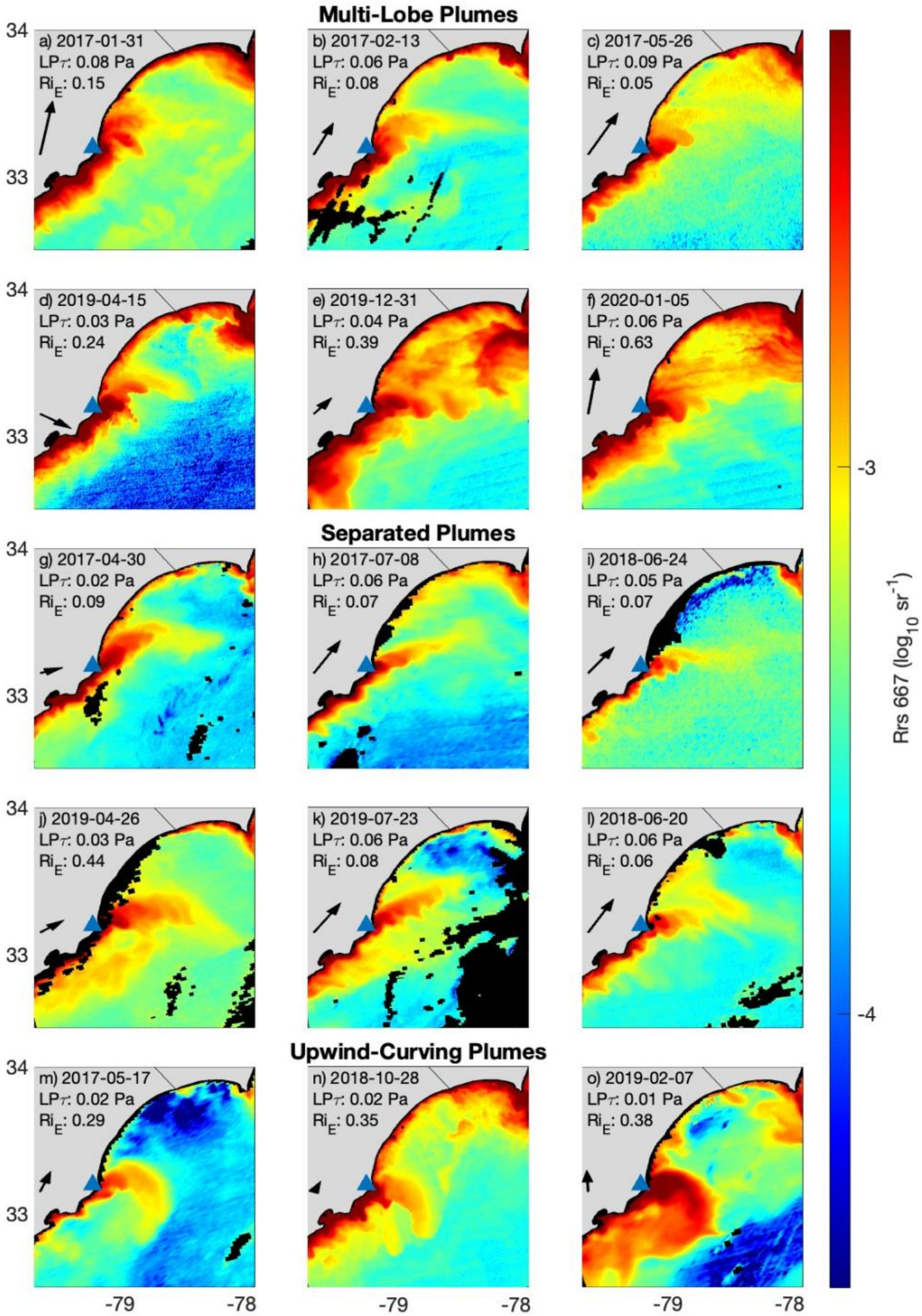

Figure 4. Remote sensing reflectance (Rrs) capturing suspended particulates of the plume (red-yellow) exciting Winyah Bay ('Δ'). Subplots are grouped by plume type: a-f) multi-lobe plumes, g-l) separated plumes, and m-o) curving plumes. For each plume, we show the preceding mean 3-day along shelf wind stress (LPτ), Ri_E, and wind stress vector. Due to moderate cloud cover (black color) for Aqua MODIS Rrs 667, b, c, and i show the similar SNPP VIIRS Rrs 671 nm. Minor acquisition bands are present in e, f, and h.

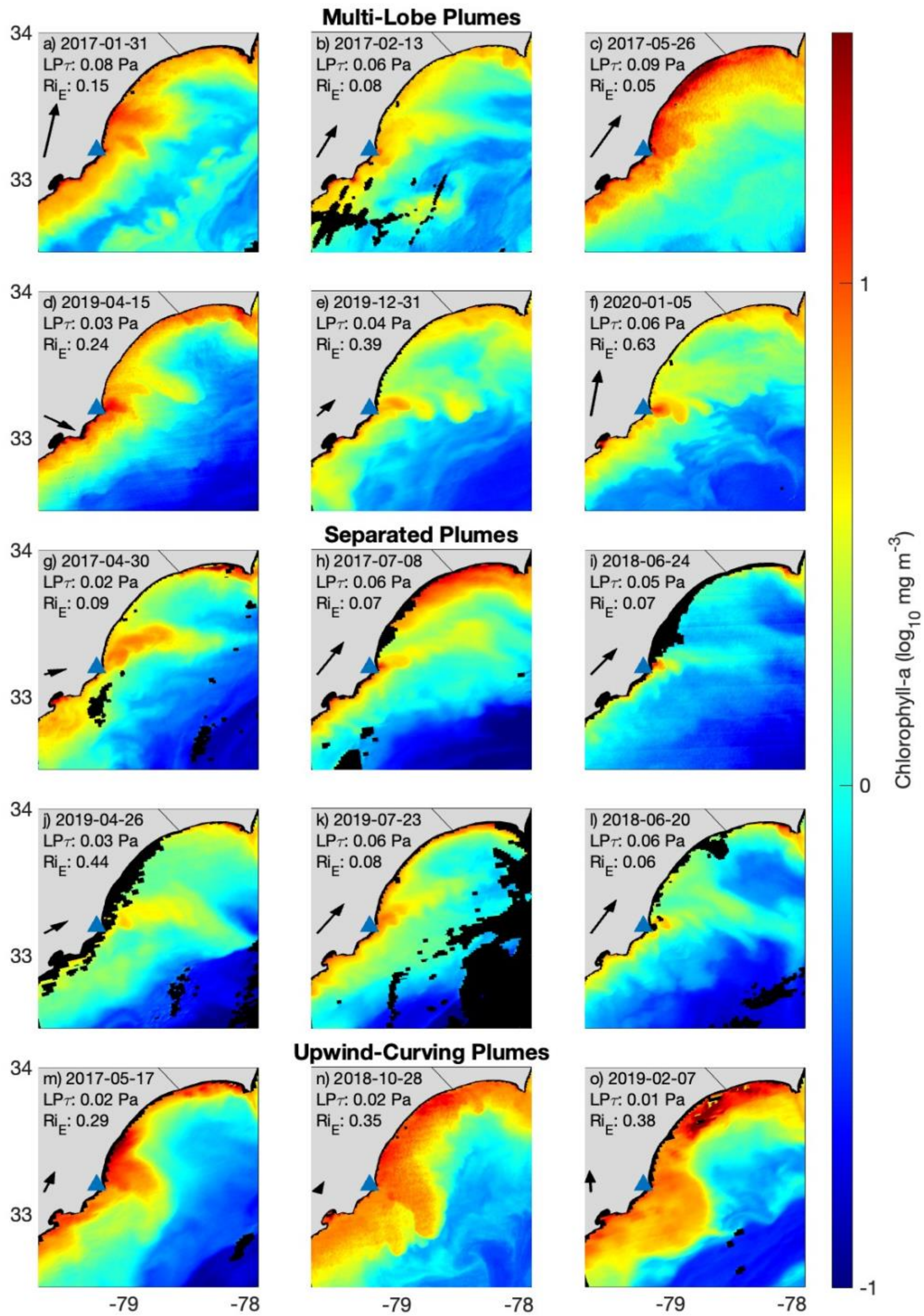

Figure 5. Satellite derived chlorophyll-a, capturing the Winyah Bay plume. Panel order, symbols, and data sources follow Figure 4.

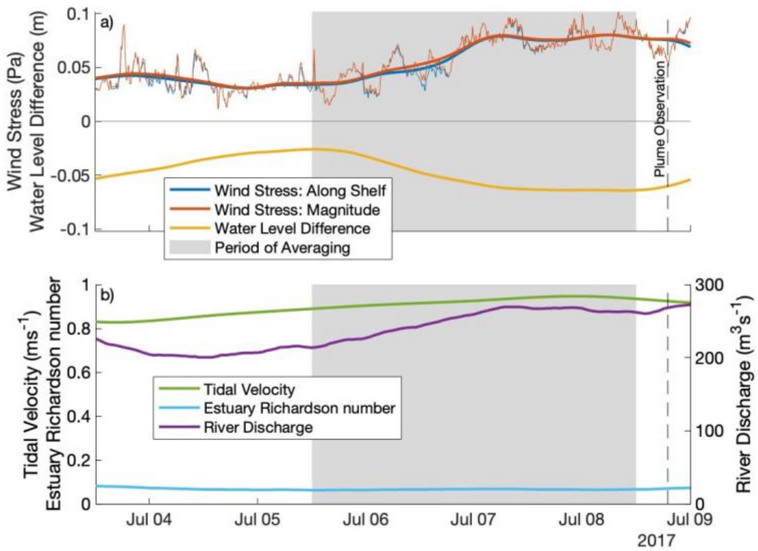

Figure 6. Timeseries of a) shelf and b) estuarine conditions for a cross-shelf plume observed on July 8, 2017 (Figures 4h, 5h). a) The along shelf wind stress is positive northeastward and a component of the total wind magnitude which is balanced by the alongshore pressure gradient, shown here using the water level difference with negative values indicating a positive northeastward slope. Different line thickness represents instantaneous (thin) and low-passed values (thick). Plume parameters are determined using the three days preceding plume observations (gray).

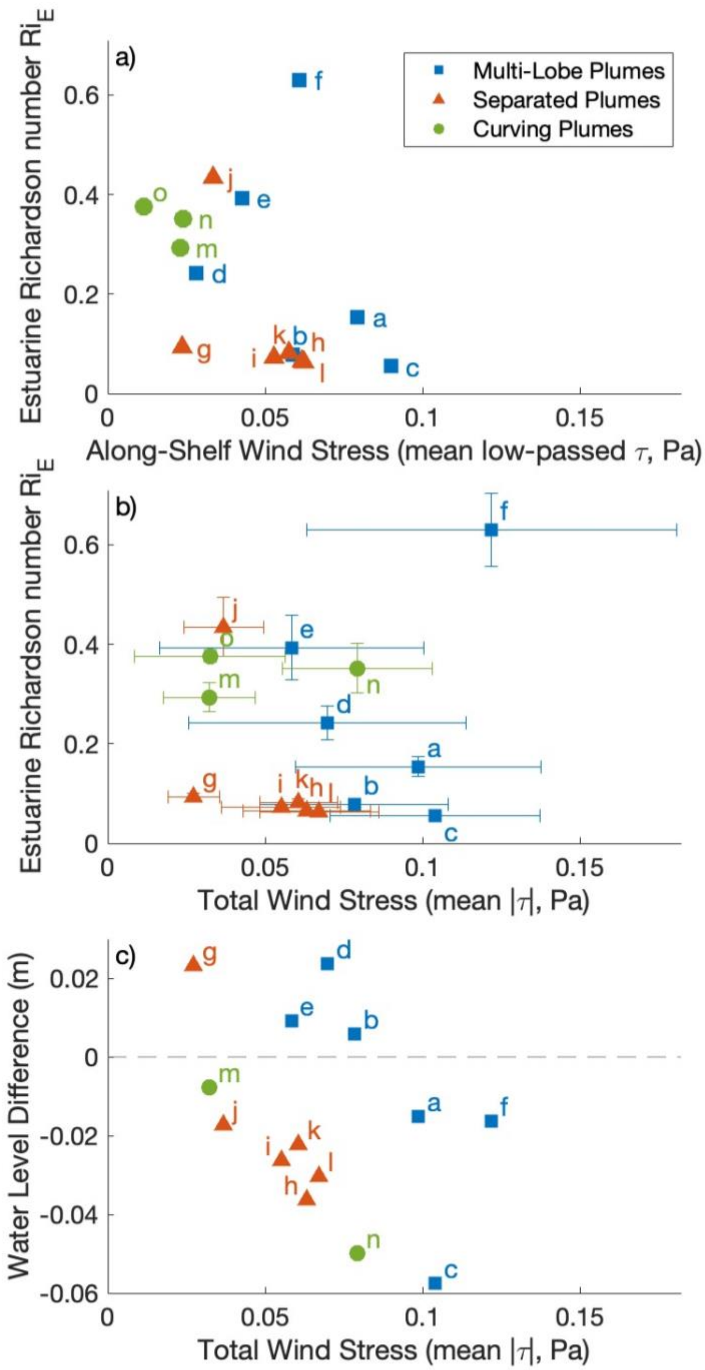

Figure 7. Plume parameters determined from the external forcing conditions are compared. Along-shelf water level difference represents the alongshore pressure gradient. Letters coordinate with Figures 4 and 5 panels; bars (b) show standard deviations. In (c), an upwind curving plume observation (2019-02-07; letter "o") is not shown because of a water-level data gap.

Figure 8. Higher-resolution satellite imagery capturing details of the plume structure on four select days: a) April 26, 2019 (Sentinel-2, 15:49 UTC), case j; b) October 28, 2018 (LANDSAT-8, 15:48 UTC), case n; and c) February 11, 2017 (LANDSAT-8, 15:54 UTC), 2 days proceeding case b. Images combine data from red, green, and blue wavelength bands, and have a spatial resolution of 10 m (Sentinel) or 30 m (Landsat).

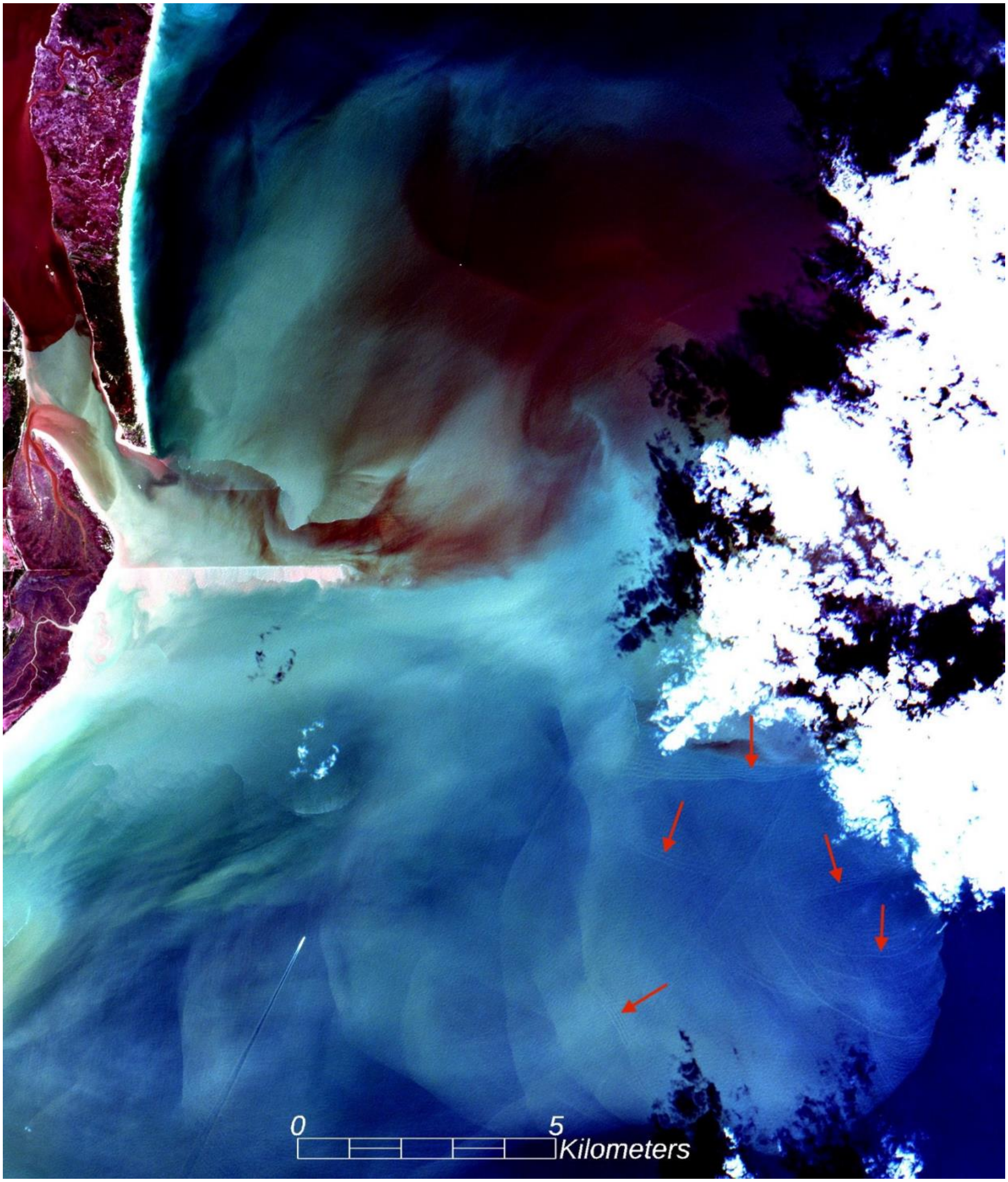

Figure 9. Same as Figure 8a, but for March 11, 2020 (Sentinel-2, 15:51 UTC). Arrows indicate the local propagation direction of five distinct packets of internal waves. The generally southward propagation direction is consistent with the theoretically expected upwind radiation of internal waves (see text).

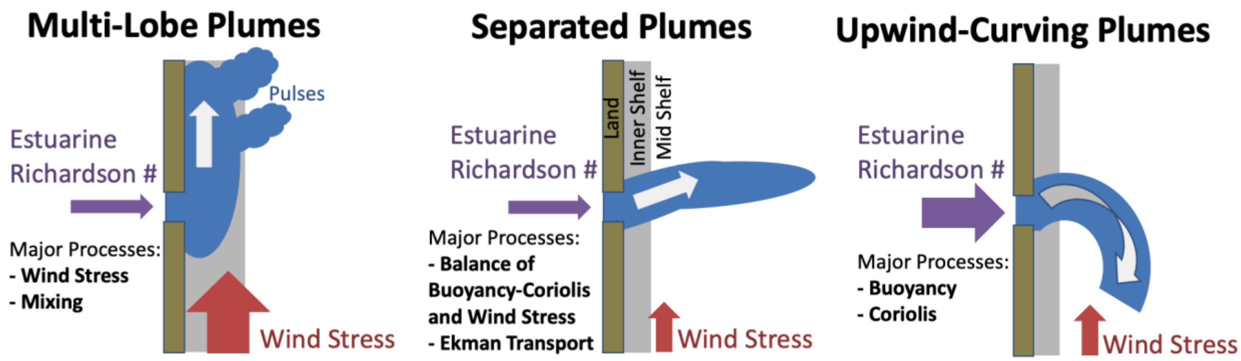

Figure 10. Diagram of the three types of cross-shelf plumes and their general forcing conditions.